

Determining the three-dimensional atomic structure of an amorphous solid

Yao Yang^{1*}, Jihan Zhou^{1*}, Fan Zhu^{1*}, Yakun Yuan^{1*}, Dillan J. Chang¹, Dennis S. Kim¹, Minh Pham², Arjun Rana¹, Xuezheng Tian¹, Yonggang Yao³, Stanley J. Osher², Andreas K. Schmid⁴, Liangbing Hu³, Peter Ercius⁴ & Jianwei Miao¹

¹*Department of Physics & Astronomy, STROBE NSF Science & Technology Center and California NanoSystems Institute, University of California, Los Angeles, CA 90095, USA.*

²*Department of Mathematics, University of California, Los Angeles, CA 90095, USA.*

³*Department of Materials Science and Engineering, University of Maryland, College Park, Maryland, 20742, USA.* ⁴*National Center for Electron Microscopy, Molecular*

Foundry, Lawrence Berkeley National Laboratory, Berkeley, CA 94720, USA.

**These authors contributed equally to this work.*

Amorphous solids such as glass are ubiquitous in our daily life and have found broad applications ranging from window glass and solar cells to telecommunications and transformer cores^{1,2}. However, due to the lack of long-range order, the three-dimensional (3D) atomic structure of amorphous solids has thus far defied any direct experimental determination without model fitting³⁻¹³. Here, using a multi-component glass-forming alloy as a proof-of-principle, we advance atomic electron tomography to determine the 3D atomic positions in an amorphous solid for the first time. We quantitatively characterize the short-range order (SRO) and medium-range order (MRO) of the 3D atomic arrangement. We find that although the 3D atomic packing of the SRO is geometrically disordered, some SROs connect with each other to form crystal-like superclusters and give rise to the MRO. We identify four crystal-like MROs – face-centred cubic, hexagonal close-packed, body-centered

25 **cubic and simple cubic – coexisting in the amorphous sample. These observations**
26 **provide direct experimental evidence to support the general framework of the**
27 **efficient cluster packing model^{8,10-12,20}. Looking forward, we anticipate this**
28 **experiment will open the door to determining the 3D atomic coordinates of various**
29 **amorphous solids, whose impact on non-crystalline solids may be comparable to the**
30 **first 3D crystal structure solved by x-ray crystallography over a century ago¹⁴.**

31 Since the first discovery in 1960¹⁵, metallic glasses have been actively studied for
32 fundamental interest and practical applications^{7-12,16-20}. However, due to their disordered
33 structure, the 3D atomic arrangement of metallic glasses cannot be determined by
34 crystallography²¹. Over the years, a number of experimental and computational methods
35 have been used to study the metallic glass structure, such as x-ray/neutron diffraction^{22,23},
36 x-ray absorption fine structure⁹, high-resolution transmission electron microscopy²⁴,
37 fluctuation electron microscopy²⁵, angstrom- and nano-beam electron diffraction^{13,26,27},
38 nuclear magnetic resonance²⁸, density functional theory²⁹, molecular dynamics
39 simulations³⁰⁻³³ and reverse Monte Carlo modelling^{9,25}. Despite all these developments,
40 however, there was no experimental method available to directly determine all the 3D
41 atomic positions in metallic glass samples. One experimental method that can in principle
42 solve this long-standing problem is atomic electron tomography (AET)^{34,35}. AET
43 combines high-resolution tomographic tilt series with advanced iterative algorithms to
44 resolve the 3D atomic structure of materials without assuming crystallinity, which has
45 been applied to image grain boundaries, anti-phase boundaries, stacking faults,
46 dislocations, point defects, chemical order/disorder, atomic-scale ripples, bond distortion
47 and strain tensors with unprecedented 3D detail³⁶⁻⁴¹. More recently, 4D (3D + time) AET
48 has been developed to observe crystal nucleation at atomic resolution, showing that early

49 stage nucleation results are inconsistent with classical nucleation theory⁴². Here, we use
50 an amorphous sample of glass-forming alloy as a model and advance AET to determine
51 its 3D atomic positions with a precision of 21 picometers.

52 **3D atomic positions in a glass-forming alloy**

53 The samples were synthesized by a carbothermal shock technique with a high cooling
54 rate (Extended Data Fig. 1a, Supplementary video 1 and Methods), which was used to
55 create high entropy alloy nanoparticles with multi-metal components⁴³. The energy-
56 dispersive X-ray spectroscopy data show the nanoparticles are composed of eight
57 elements: Co, Ni, Ru, Rh, Pd, Ag, Ir and Pt (Extended Data Fig. 1b-k). Tomographic tilt
58 series were acquired from seven nanoparticles using a scanning transmission electron
59 microscope with an annular dark-field detector (Extended Data Table 1). While most of
60 the nanoparticles are crystalline or polycrystalline, particles 1 and 2 have disordered
61 structure (Extended Data Fig. 2). In this study, we focus on the most disordered
62 nanoparticle (particle 1), from which a tilt series of 55 images was acquired (Fig. 1a and
63 Extended Data Fig. 3). Although some crystalline features are present in several images,
64 the 2D power spectra calculated from the images show the amorphous halo.

65 After pre-processing and image denoising, the tilt series was reconstructed and
66 the 3D atomic positions were traced and classified (Fig. 1c, d, Supplementary Video 2
67 and Methods). Since the image contrast in the 3D reconstruction depends on the atomic
68 number⁴⁰⁻⁴², presently AET is only sensitive enough to classify the eight elements into
69 three different types: Co and Ni as type 1, Ru, Rh, Pd and Ag as type 2, and Ir and Pt as
70 type 3. After atom classification, we obtained the 3D atomic model of the nanoparticle,
71 consisting of 8322, 6896 and 3138 atoms for type 1, 2 and 3, respectively. To verify the
72 reconstruction, atom tracing and classification procedure, we calculated 55 images from

73 the experimental atomic model using multislice simulations (Methods). Extended Data
74 Fig. 4c and d shows the consistency between the experimental and calculated images. We
75 then applied the reconstruction, atom tracing and classification procedure to obtain a new
76 3D atomic model from the 55 multislice images. By comparing the two models, we
77 estimated that 97.37% of atoms were correctly identified with a 3D precision of 21 pm
78 (Methods and Extended Data Fig. 4e).

79 Figure 1e and Supplementary video 3 show the experimental 3D atomic model of
80 the nanoparticle with type 1, 2 and 3 atoms in green, blue and red, respectively. To
81 quantitatively characterize the atomic structure, we employed the local bond orientational
82 order (BOO) parameters to distinguish between the disordered, face-centred cubic (fcc),
83 hexagonal close-packed (hcp) and body-centered cubic (bcc) structures (Methods). Figure
84 1f shows the local BOO parameters of all the atoms in the nanoparticle, indicating the
85 majority of atoms severely deviate from the fcc, hcp and bcc crystal structures. For a
86 comparison, the local BOO parameters of all the seven nanoparticles are shown in
87 Extended Data Fig. 2h-n. To separate crystal nuclei from the amorphous structure, we
88 used the normalized BOO parameter to identify the crystal nuclei (Methods). By choosing
89 the criterion of the normalized BOO parameter ≥ 0.5 (Extended Data Fig. 2o), we
90 identified 15.46% of the total atoms forming crystal nuclei in the nanoparticle (Extended
91 Data Fig5a), which contribute to the crystalline features observed in several images
92 (Extended Data Fig. 3). The characteristic width of the crystalline-amorphous interface
93 was determined to be 3.69 Å in the nanoparticle (Methods), indicating that the crystal
94 nuclei have a minimal effect on the structural disorder beyond a few angstroms. In the
95 following sections, we focus on the analysis of the disordered atoms with the normalized
96 BOO parameter < 0.5 .

97 Figure 1g shows the pair distribution function (PDF) of the amorphous structure
98 of the 3D atomic model (Methods), where the weak second-peak splitting is consistent
99 with previous observation in high entropy bulk metallic glasses⁴⁴. The ratios of the
100 second, third, fourth and fifth to the first peak position are 1.74, 1.99, 2.64 and 3.51,
101 respectively, which are in good agreement with those of metallic glasses^{45,46}. The partial
102 PDFs between type 1, 2 and 3 atoms are shown in Fig. 1h. By fitting a Gaussian to the
103 first peaks in the partial PDFs, we determined the type 11, 12, 13, 22, 23 and 33 bond
104 lengths to be 2.59, 2.71, 2.78, 2.72, 2.75 and 2.9 Å, respectively. In particular, the partial
105 PDF for the type 33 pairs (the yellow curve) exhibits a unique feature with the second
106 peak higher than the first peak, indicating that the majority of type 3 atoms are distributed
107 beyond the SRO.

108 **The short-range order**

109 To determine the SRO in the glass-forming nanoparticle, we used the Voronoi tessellation
110 to characterize the local atomic arrangement⁶. This method identifies the nearest
111 neighbour atoms around each central atom to form a Voronoi polyhedron, which is
112 designated by a Voronoi index $\langle n_3, n_4, n_5, n_6 \rangle$ with n_i denoting the number of i -edged
113 faces. Figure 2a shows the ten most abundant Voronoi polyhedra in the nanoparticle with
114 a fraction ranging from 5.02% to 1.72%, most of which are geometrically disordered and
115 commonly observed in model metallic glasses¹¹ such as $\langle 0,4,4,3 \rangle$, $\langle 0,3,6,3 \rangle$, $\langle 0,4,4,2 \rangle$
116 and $\langle 0,3,6,2 \rangle$ (Fig. 2b). To examine the effect of the precision of AET on the Voronoi
117 analysis, we added the experimental error (Extended Data Fig. 4e) to a Cu₆₅Zr₃₅ metallic
118 glass model obtained from molecular dynamics simulations. By comparing the Voronoi
119 polyhedra with and without the error, we found that the precision of AET has only a small
120 effect on the Voronoi tessellation (Methods). This result suggests that the small fractions

121 of the Voronoi polyhedra in the glass-forming nanoparticle are mainly due to its poor
122 glass forming ability^{11,18}.

123 Figure 2c shows the local symmetry distribution of all the faces of the Voronoi
124 polyhedra. The 3-, 4-, 5- and 6-edged faces account for 3.27%, 29.14%, 43.91% and
125 23.67%, respectively, revealing that 5-edged faces are most abundant in the SRO. But
126 only 7.03% of all the Voronoi polyhedra are distorted icosahedra, including Voronoi
127 indices $\langle 0,0,12,0 \rangle$, $\langle 0,1,10,2 \rangle$, $\langle 0,2,8,2 \rangle$ and $\langle 0,2,8,1 \rangle$. This observation indicates that
128 most 5-edged faces do not form distorted icosahedra in this glass-forming nanoparticle.
129 From the Voronoi tessellation, we also calculated the distribution of the coordination
130 number (CN) (Fig. 2d and Methods), where the average CNs of types 1, 2 and 3 atoms
131 are 11.97, 12.02 and 12.41, respectively. Based on the partial CNs (Extended Data Fig.
132 5b), we quantified the chemical SRO using the Warren–Cowley parameters (Methods),
133 indicating that the type 11 and 23 bonds are favoured, but the type 12 and 33 bonds are
134 unfavoured. These results are consistent with the observations of the shortening of the
135 type 11 and 23 bonds and the lengthening of the type 12 and 33 bonds (Methods).

136 **The medium-range order**

137 While the MRO in metallic glasses is broadly defined as the nanometre-scale structural
138 organization beyond the SRO^{8-13,20,25,26,31}, in this work we focused on the investigation of
139 the MRO in the framework of the efficient cluster packing model^{8,12}. This model
140 hypothesizes that solute atoms are surrounded by randomly-positioned solvent atoms to
141 form solute-centred clusters, which are densely packed to constitute crystal-like MROs
142 in metallic glasses. To quantitatively test this model with experimental data, we analysed
143 the partial PDF of type 33 atom pairs (Fig. 1h, the yellow curve) and observed that the
144 highest peak is at 4.77 Å and 1.49 times higher than the nearest neighbour peak. We found

145 that 85.47% of type 3 atoms are distributed in the second coordination shell (Extended
146 Data Fig. 5c and Methods), which is between the first (3.86 Å) and the second minimum
147 (6.08 Å) of the PDF curve (Fig. 1g). These type 3 atoms act as solute atoms and are
148 surrounded mainly by type 1 and 2 solvent atoms to form solute-centred clusters.
149 Extended Data Fig. 5d shows the ten most abundant Voronoi polyhedra of these clusters.
150 The solute-centred clusters connect with each other by sharing one (a vertex), two (an
151 edge) and three atoms (a face) as well as protrude into each other by sharing four and five
152 atoms (Fig. 3a-e). Figure 3f shows the statistical distribution of the number of the solute-
153 centred cluster pairs, which share from one to five atoms.

154 To locate the MRO in the glass-forming nanoparticle, we implemented a breadth-
155 first search algorithm to look for the fcc-, hcp-, bcc-, simple cubic (sc-) and icosahedral-
156 like structures of the solute centres (Methods). This algorithm globally searches for the
157 MRO with a maximum number of solute centres. Each MRO is defined to have five or
158 more solute centres with each solute centre falling within a 0.75 Å radius to the fcc, hcp,
159 bcc, sc lattice or icosahedral vertices. We found that four types of MROs (fcc-, hcp-, bcc-
160 and sc-like) coexist in the sample (Methods). Although we did not observe icosahedral-
161 like MROs in this sample, our work does not rule out its existence in other metallic
162 glasses⁹. Figure 3g shows the histogram of the four types of MROs as a function of the
163 size, where the inset illustrates the fraction of the solute centre atoms in the four types of
164 MROs. Figure 3h and Supplementary Video 4 show the 3D distribution of MROs with
165 each having eight solute centres or more. To verify our analysis, we also searched for
166 MROs with a 1 Å and 0.5 Å radius cut-off and observed the coexistence of the four types
167 of MROs with different cut-off radii (Extended Data Figs. 6 and 7).

168 Next, we quantitatively characterized MROs with a 0.75 Å radius cut-off. Figure
169 4a and b show the length and volume distribution of the MROs in the glass-forming
170 nanoparticle. The average length of the fcc-, hcp-, bcc- and sc-like MROs was measured
171 to be 2.27 ± 0.50 , 2.40 ± 0.42 , 2.07 ± 0.38 , 2.11 ± 0.48 nm, respectively, with the
172 corresponding average volume of 1.80 ± 0.64 , 1.96 ± 0.53 , 1.63 ± 0.46 and 1.96 ± 0.74
173 nm³. Figure 5a, c, e and g show four representative fcc-, hcp-, bcc- and sc-like MROs, in
174 which the individual solute-centred clusters are randomly oriented. To better visualize
175 these MROs, the solute centres are orientated along the fcc, hcp, bcc and sc zone axes
176 (Fig. 5b, d, f and h), showing that the 3D shapes of the MROs are anisotropic. We
177 calculated the partial PDFs of all the fcc-, hcp-, bcc- and sc-like solute centres in the glass-
178 forming nanoparticle and their corresponding maximum peak positions are at 4.62, 4.77,
179 4.82 and 3.88 Å, respectively (Fig. 4c). These peak positions represent the average nearest
180 neighbour distances of the solute centres in the four crystal-like MROs and the broadened
181 peaks signify the severe deviation from the crystal lattices. Compared with the other three
182 partial PDFs, the partial PDF of the sc-like MROs has two peaks and the ratio of the
183 second to the first peak position is about $\sqrt{2}$ (Fig. 4c, the purple curve), which
184 corresponds to the ratio of the diagonal to the side length of a square. The shorter nearest
185 neighbour distance of the sc-like MROs compared to the other three crystal-like MROs
186 indicates that the sc-like solute-centred clusters are more closely connected with their
187 neighbours. Figure 4d shows the distribution of sharing one, two, three, four and five
188 atoms between neighbouring solute-centred clusters for the four types of MROs,
189 confirming that the solute-centred clusters in the sc-like MROs tend to share more atoms
190 with their neighbours than those in other types of MROs.

191 Our quantitative analysis of the SRO and MRO in a multi-component glass-
192 forming nanoparticle provides direct experimental evidence to support the general
193 framework of the efficient cluster packing model^{8,10-12,20}, that is, solute-centred clusters
194 are densely packed in some parts of the sample to form crystal-like MROs. We observed
195 the chemical SRO, the bond shortening and lengthening, and the coexistence of fcc-, hcp-
196 , bcc- and sc-like MROs in the glass-forming nanoparticle. By quantifying their length,
197 volume and 3D structure, we found that the MROs not only has a large variation in length
198 and volume, but also severely deviates from the crystal lattices (Fig. 4c). As the size of
199 the MROs is comparable to that of shear transformation zones in metallic glasses^{11,20,47,48},
200 we expect that AET could also be applied to determine the 3D atomic structures related
201 to shear transformation zones and link the structure and properties of metallic glasses¹¹.

202 **Outlook**

203 Over the last century, crystallography has been broadly applied to determine the 3D
204 atomic structure of crystalline samples²¹. The quantitative 3D structural information has
205 been fundamental to the development of many scientific fields. However, for amorphous
206 solids, their 3D structure has been primarily inferred from experimental data, where either
207 the average statistical structural information can be obtained or model fitting is required
208 to analyse the local atomic order⁸⁻¹³. These qualitative approaches have hindered our
209 fundamental understanding of the 3D structure of amorphous solids and related
210 phenomena such as the crystal-amorphous phase transition and the glass transition^{11,49,50}.
211 Here, we demonstrate the ability to directly determine the 3D atomic structure of an
212 amorphous solid using AET, which enables us to quantitatively analyse the SRO and
213 MRO at the single-atom level. Although we focus on a multi-component glass-forming
214 nanoparticle in this study, this method is generally applicable to different sample

215 geometries such as thin films and extended objects (Extended Data Figs. 8 and 9,
216 Methods). Thus, we expect that this work could open a new era in determining the 3D
217 structure of a wide range of amorphous solids.

218 **References**

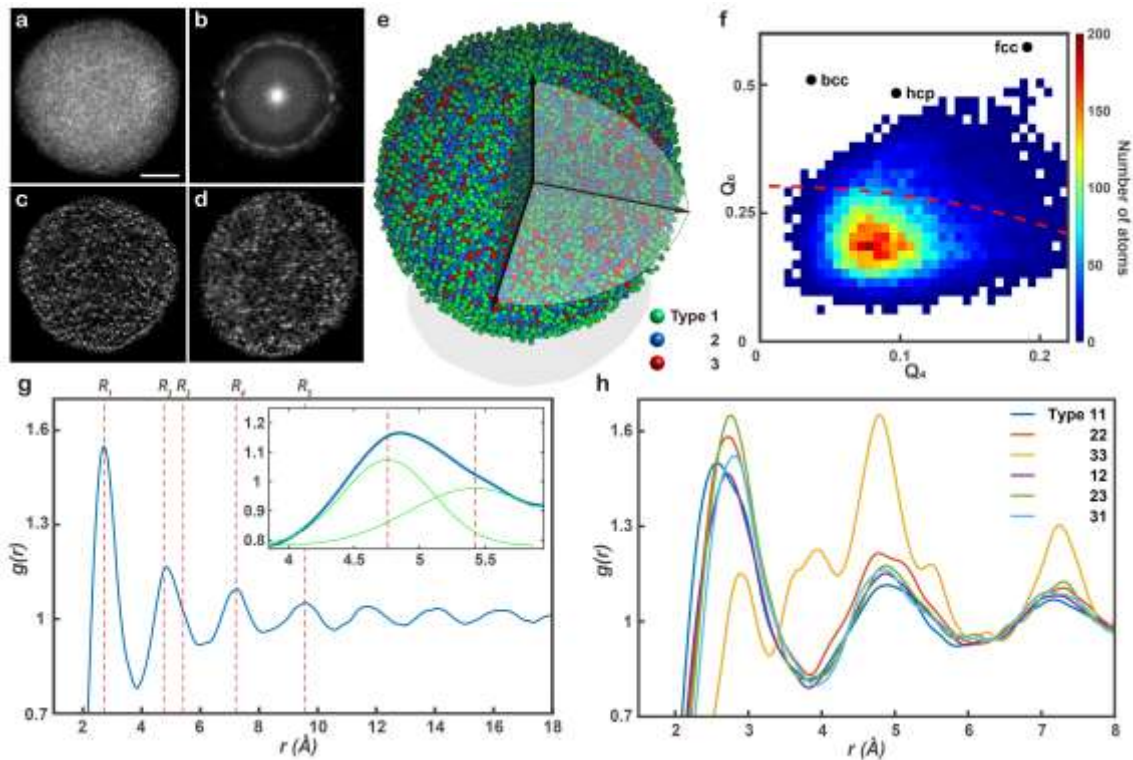
- 219 1. Zallen, R. *The Physics of Amorphous Solids* (Wiley, 1998).
- 220 2. Elliott, S. R. *Physics of Amorphous Materials* (Harlow, Essex, England: Longman
221 Scientific & Technical, 1990).
- 222 3. Zachariasen, W. H. The atomic arrangement in glass. *J. Am. Chem. Soc.* **54**, 3841-3851
223 (1932).
- 224 4. Bernal, J. D. & Mason, J. Packing of spheres: co-ordination of randomly packed
225 spheres. *Nature* **188**, 910-911 (1960).
- 226 5. Scott, G. D. Packing of equal spheres. *Nature* **188**, 908-909 (1960).
- 227 6. Finney, J. L. Random packings and structure of simple liquids. 1. Geometry of random
228 close packing. *Proc. Roy Soc. Lond. Ser. A - Math. Phys. Sci.* **319**, 479-493 (1970).
- 229 7. Nelson, D. R. & Spaepen, F. Polytetrahedral order in condensed matter. *Solid State*
230 *Phys.* **42**, 1-90 (1989).
- 231 8. Miracle, D. B. A structural model for metallic glasses. *Nat. Mater.* **3**, 697-702 (2004).
- 232 9. Sheng, H. W., Luo, W. K., Alamgir, F. M., Bai, J. M. & Ma, E. Atomic packing and
233 short-to-medium-range order in metallic glasses. *Nature* **439**, 419-425 (2006).
- 234 10. Miracle, D. B., Egami, T., Flores, K. M. & Kelton, K. F. Structural aspects of metallic
235 glasses. *MRS Bull.* **32**, 629-634 (2007).
- 236 11. Cheng, Y. Q. & Ma, E. Atomic-level structure and structure-property relationship in
237 metallic glasses. *Prog. Mater. Sci.* **56**, 379-473 (2011).
- 238 12. Miracle, D. B. A Physical Model for Metallic Glass Structures: An Introduction and
239 Update. *JOM* **64**, 846-855(2012).

- 240 13. Hirata, A. et al. Geometric frustration of icosahedron in metallic glasses. *Science* **341**,
241 376-379 (2013).
- 242 14. Bragg, W. L. The structure of some crystals as indicated by their diffraction of X-rays.
243 *Proc. R. Soc. London Ser. A* **89**, 248-277 (1913).
- 244 15. Klement Jun, W., Willens, R. H. & Duwez, P. Non-crystalline structure in solidified
245 gold–silicon alloys. *Nature* **187**, 869-870 (1960).
- 246 16. Greer, A. L. Metallic glasses. *Science* **267**, 1947-1953 (1995).
- 247 17. Peker, A. & Johnson, W. L. A highly processable metallic glass: $Zr_{41.2}Ti_{13.8}Cu_{12.5}Ni_{10.0}Be_{22.5}$. *Appl. Phys. Lett.* **63**, 2342-2344 (1993).
- 248
- 249 18. Inoue, A. Stabilization of metallic supercooled liquid and bulk amorphous alloys. *Acta*
250 *Mater.* **48**, 279-306 (2000).
- 251 19. Wang, W. H., Dong, C. & Shek. C. H. Bulk metallic glasses. *Mater. Sci. Eng.: R: Rep.*
252 **44**, 45-89 (2004).
- 253 20. Chen, M.W. A brief overview of bulk metallic glasses. *NPG Asia Mater.* **3**, 82-90
254 (2011).
- 255 21. Crystallography at 100. *Science* **343**, 1091-1116 (2014).
- 256 22. Egami, T. & Billinge, S. J. L. *Underneath the Bragg Peaks: Structural Analysis of*
257 *Complex Materials*. (Pergamon Materials Series, v.7, 2003).
- 258 23. Kelton, K. F. et al. First X-ray scattering studies on electrostatically levitated metallic
259 liquids: demonstrated influence of local icosahedral order on the nucleation barrier.
260 *Phys. Rev. Lett.* **90**, 195504 (2003).
- 261 24. Zhong, L., Wang, J., Sheng, H., Zhang, Z. & Mao, S. X. Formation of monatomic
262 metallic glasses through ultrafast liquid quenching. *Nature* **512**, 177-180 (2014).
- 263 25. Hwang, J. et al. Nanoscale structure and structural relaxation in $Zr_{50}Cu_{45}Al_5$ bulk
264 metallic glass. *Phys. Rev. Lett.* **108**, 195505 (2012).
- 265 26. Hirata, A. et al. Direct observation of local atomic order in a metallic glass. *Nat. Mater.*
266 **10**, 28-33 (2011).

- 267 27. Pekin, T.C. et al. Direct measurement of nanostructural change during in situ
268 deformation of a bulk metallic glass. *Nat. Commun.* **10**, 2445 (2019).
- 269 28. Tang, X. P., Geyer, U., Busch, R., Johnson, W. L. & Wu, Y. Diffusion mechanisms in
270 metallic supercooled liquids and glasses. *Nature* **402**, 160-162 (1999).
- 271 29. Sachdev, S. & Nelson, D. R. Order in metallic glasses and icosahedral crystals. *Phys.*
272 *Rev. B* **32**, 4592-4606 (1985).
- 273 30. Tang, C., & Harrowell, P. Anomalously slow crystal growth of the glass-forming alloy
274 CuZr. *Nat. Mater.* **12**, 507-511 (2013).
- 275 31. Cheng, Y. Q., Ma, E. & Sheng, H. W. Atomic level structure in multicomponent bulk
276 metallic glass. *Phys. Rev. Lett.* **102**, 245501 (2009).
- 277 32. Hu, Y. C., Li, F. X., Li, M. Z., Bai, H. Y. & Wang, W. H. Five-fold symmetry as
278 indicator of dynamic arrest in metallic glass-forming liquids. *Nat. Commun.* **6**, 8310
279 (2015).
- 280 33. Ding, J. & Ma, E. Computational modeling sheds light on structural evolution in
281 metallic glasses and supercooled liquids. *Npj Comput. Mater.* **3**, 9 (2017).
- 282 34. Scott, M. C. et al. Electron tomography at 2.4-angstrom resolution. *Nature* **483**, 444-
283 447 (2012).
- 284 35. Miao, J., Ercius, P. & Billinge, S. J. L. Atomic electron tomography: 3D structures
285 without crystals. *Science* **353**, aaf2157 (2016).
- 286 36. Chen, C.-C. et al. Three-dimensional imaging of dislocations in a nanoparticle at atomic
287 resolution. *Nature* **496**, 74-77 (2013).
- 288 37. Goris, B. et al. Three-Dimensional Elemental Mapping at the Atomic Scale in
289 Bimetallic Nanocrystals. *Nano Lett.* **13**, 4236-4241 (2013).
- 290 38. Xu, R. et al. Three-dimensional coordinates of individual atoms in materials revealed by
291 electron tomography. *Nat. Mater.* **14**, 1099-1103 (2015).

- 292 39. Haberfehlner, G. et al. Formation of bimetallic clusters in superfluid helium
293 nanodroplets analysed by atomic resolution electron tomography. *Nat. Commun.* **6**,
294 8779 (2015).
- 295 40. Yang, Y. et al. Deciphering chemical order/disorder and material properties at the
296 single-atom level. *Nature* **542**, 75-79 (2017).
- 297 41. Tian, X. et al. Correlating the three-dimensional atomic defects and electronic
298 properties of two-dimensional transition metal dichalcogenides. *Nat. Mater.* **19**, 867–
299 873 (2020).
- 300 42. Zhou, J. et al. Observing crystal nucleation in four dimensions using atomic electron
301 tomography. *Nature* **570**, 500-503 (2019).
- 302 43. Yao, Y. et al. Carbothermal shock synthesis of high-entropy-alloy nanoparticles. *Science*
303 **359**, 1489-1494 (2018).
- 304 44. Kim, J. Y. et al. Utilization of high entropy alloy characteristics in Er-Gd-Y-Al-Co high
305 entropy bulk metallic glass. *Acta Mater.* **155**, 350-361 (2018).
- 306 45. Liu, X. J. et al. Metallic liquids and glasses: atomic order and global packing. *Phys.*
307 *Rev. Lett.* **105**, 155501 (2010).
- 308 46. Wu, Z. W., Li, M. Z., Wang, W. H. Liu, K.X. Hidden topological order and its
309 correlation with glass-forming ability in metallic glasses. *Nat. Commun.* **6**, 6035 (2015).
- 310 47. Spaepen, F. A microscopic mechanism for steady state inhomogeneous flow in metallic
311 glasses. *Acta Metall.* **25**, 407-415 (1977).
- 312 48. Argon A. S. Plastic-deformation in metallic glasses. *Acta Metall.* **27**, 47–58 (1979).
- 313 49. Johnson, W. L. Thermodynamic and kinetic aspects of the crystal to glass
314 transformation in metallic materials. *Prog. Mater. Sci.* **30**, 81-134 (1986).
- 315 50. Debenedetti, P. G. & Stillinger, F. H. Supercooled liquids and the glass transition.
316 *Nature* **410**, 259-267 (2001).

317 **Figures and figure legends**



318

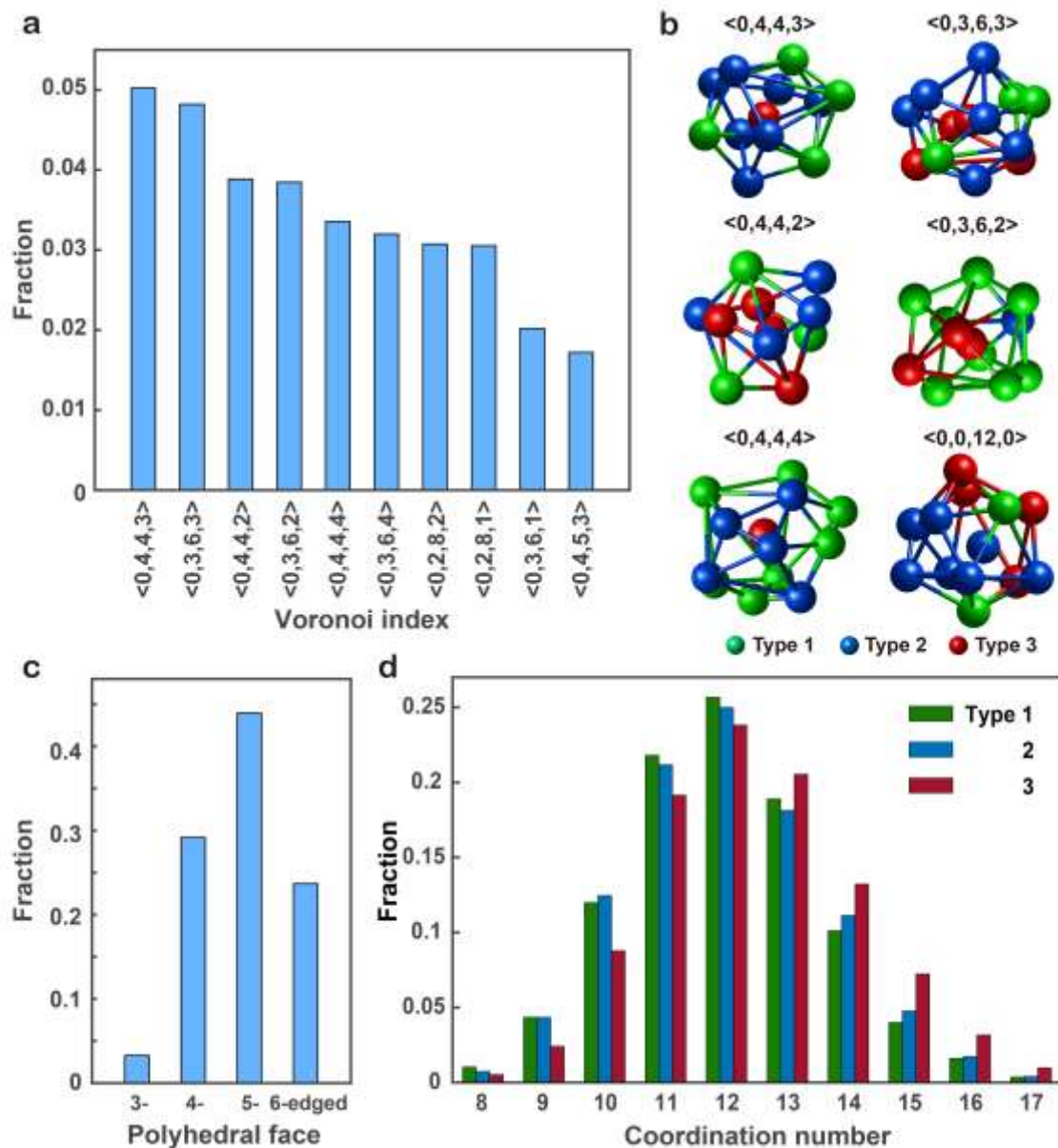
319 **Figure 1 | Determining the 3D atomic structure of a multi-component glass-forming**320 **nanoparticle with AET. a**, A representative experimental image, where some crystalline321 features are visible. Scale bar, 2 nm. **b**, Average 2D power spectrum of 55 experimental322 images (Extended Data Fig. 3), showing the amorphous halo. **c**, **d**, Two 2.4-Å-thick slices323 of the 3D reconstruction in the *xy*- and *yz*-plane, respectively, where the majority of type324 3 atoms (bright dots) are distributed in the second coordination shell. **e**, Experimental 3D325 atomic model of the glass-forming nanoparticle. **f**, The local BOO parameters of all the

326 atoms in the nanoparticle. Based on the criterion of the normalized BOO parameter < 0.5

327 (the dashed red curve), 84.54% of the total atoms are disordered. **g**, The PDF of the328 disordered atoms with the first, second, third, fourth and fifth peak positions (R_1 , R_2 , R_3 ,329 R_4 and R_5) at 2.73, 4.76, 5.42, 7.22 and 9.57 Å, respectively. The inset shows the second-330 peak splitting with a Gaussian fit. **h**, The partial PDFs between type 1, 2 and 3 atoms,

331 consisting of 6 pairs - types 11, 12, 13, 22, 23 and 33. The partial PDF for the type 33

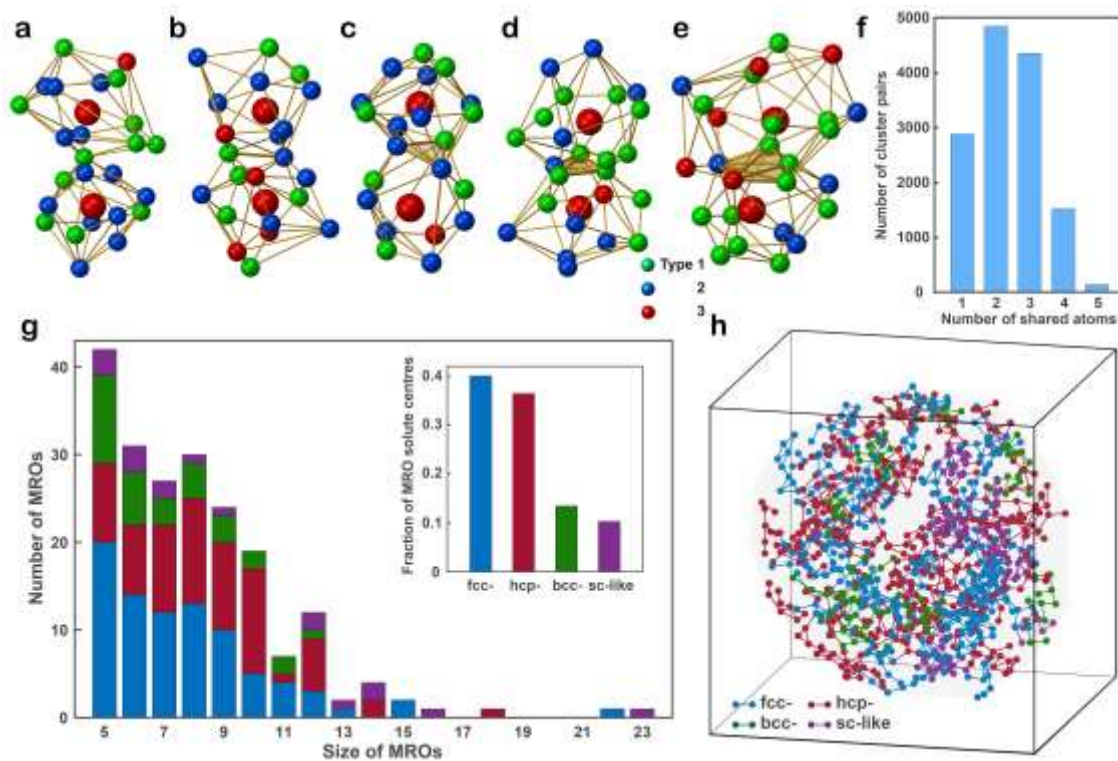
332 pairs (the yellow curve) shows a unique feature with a higher second peak than the first
 333 peak.



334

335 **Figure 2 | The short-range order of the glass-forming nanoparticle. a**, Ten most
 336 abundant Voronoi polyhedra in the nanoparticle. **b**, Six representative Voronoi polyhedra,
 337 where $\langle 0,4,4,3 \rangle$, $\langle 0,3,6,3 \rangle$, $\langle 0,4,4,2 \rangle$ and $\langle 0,3,6,2 \rangle$ are the four highest fraction Voronoi
 338 indices, $\langle 0,4,4,4 \rangle$ shows a severely distorted polyhedron, and $\langle 0,0,12,0 \rangle$ represents an
 339 icosahedron. **c**, The 3-, 4-, 5- and 6-edged face distribution of all the Voronoi polyhedra,

340 where the 5-edged faces are the most abundant (43.91%). **d**, The coordination number
 341 distributions for type 1, 2 and 3 atoms.



342

343 **Figure 3 | The connectivity and distribution of the MROs in the glass-forming**

344 **nanoparticle. a-e**, Representative pairs of the solute-centred clusters that are connected

345 with each other by sharing one, two, three, four and five atoms, respectively, where the

346 central atom of each cluster is labelled with a large red sphere. **f**, Statistical distribution

347 of the number of the solute-centred cluster pairs, which share from one to five atoms. **g**,

348 Histogram of the four types of MROs – fcc- (in blue), hcp- (in red), bcc- (in green) and

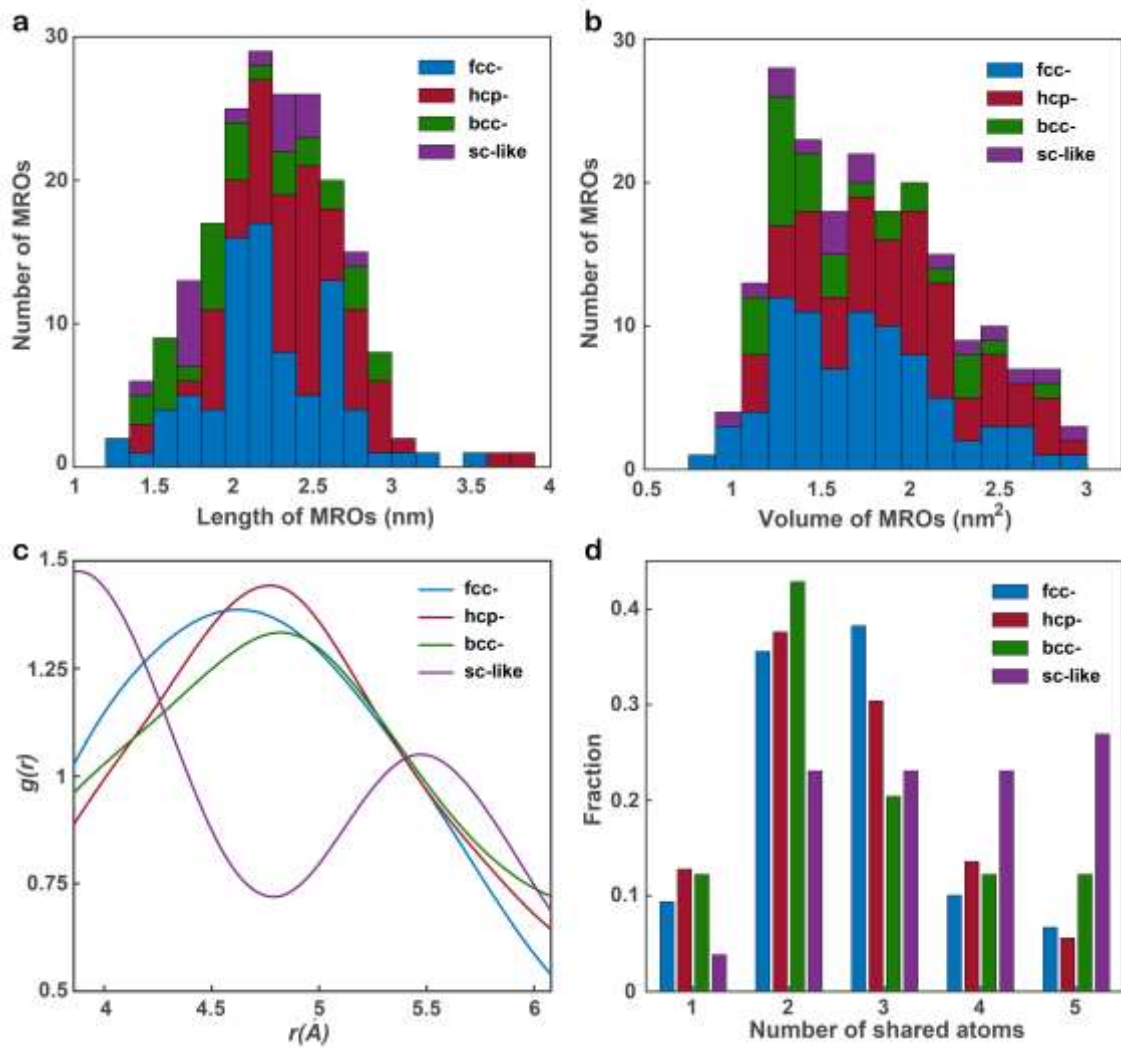
349 sc-like (in purple) – as a function of the size (i.e. the number of solute centres). The total

350 number of fcc-, hcp-, bcc- and sc-like MROs is 85, 71, 31 and 17, respectively. The inset

351 shows the fraction of the solute centre atoms in the four types of MROs. **h**, Distribution

352 of the four types of MROs with eight solute centre atoms or more, where the centre region

353 lacks of large MROs.



354

355 **Figure 4 | Quantitative characterization of MROs.** The length (a) and volume (b)

356 distribution of the four types of MROs in the glass-forming nanoparticle, where the length

357 was measured along the longest direction of each MRO. c, Partial PDFs of the fcc-, hcp-

358 , bcc- and sc-like solute centres in the glass-forming nanoparticle, where the maximum

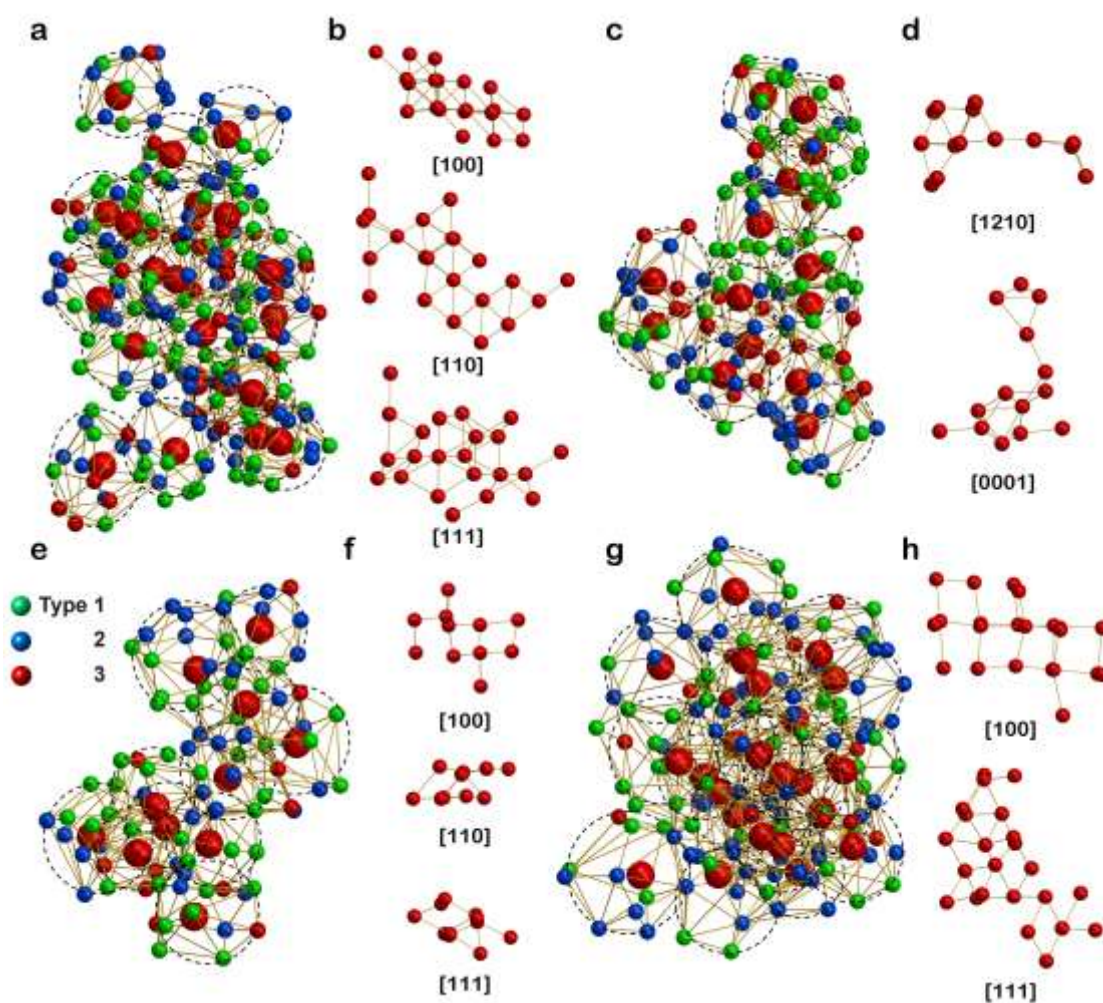
359 peak positions are located at 4.62, 4.77, 4.82 and 3.88 Å, respectively. Compared with

360 the other three partial PDFs, the partial PDF of the sc-like solute centres (the purple curve)

361 shows two peaks with the ratio of the second to the first peak position about $\sqrt{2}$. d,

362 Distribution of sharing one, two, three, four and five atoms between neighbouring solute-

363 centred clusters for the four types of MROs.



364

365 **Figure 5 | 3D atomic packing of four representative MROs.** Representative fcc- (a),
 366 hcp- (c), bcc- (e) and sc-like (g) MROs, consisting of 22, 14, 11 and 23 solute centres
 367 (large red spheres), respectively, where the individual solute-centred clusters (dashed
 368 circles) are randomly oriented. To better visualize the crystal-like MROs, the solvent
 369 atoms are removed and the solute centres are orientated along the fcc (b), hcp (d), bcc (f)
 370 and sc (h) zone axes, showing that the MROs have anisotropic 3D shapes and are severely
 371 deviate from the crystal lattices.

372 METHODS

373 **Sample preparation.** The multi-component metallic nanoparticle samples were synthesized using the
 374 thermal shock procedures published elsewhere⁴³. Individual metal salts (chlorides or their hydrate forms)

375 were dissolved in ethanol at a concentration of 0.05 mol/L. After complete dissolving with hydrochloric
376 acid, the individual salt precursor solutions with different cations were mixed and sonicated for 30 minutes.
377 The homogeneously mixed precursor solution was loaded onto the carbon substrates⁵¹ (reduced graphene
378 oxide) and heated to a temperature as high as 1,763 K for 55 milliseconds (Extended Data Fig. 1a). The
379 sample was suspended on a trench and connected with copper electrodes by silver paste for both heating
380 and effective cooling as a giant heat sink. The thermal shock synthesis was triggered by electric Joule
381 heating in an argon-filled glovebox using a Keithley 2425 SourceMeter where the high temperature and
382 duration can be effectively controlled by tuning the input power and duration. The temperature of this
383 process was monitored by a high-speed Phantom Miro M110 camera with a pixel size of 25 μm
384 (Supplementary Video 1). The cooling rate was estimated to be $\sim 5.1\text{-}6.9 \times 10^4$ K/s (Extended Data Fig. 1a),
385 which, according to previous studies, can make metallic glasses^{52,53}. The resulting nanoparticles on reduced
386 graphene oxide were dispersed in ethanol with sonication. After deposited on to 5-nm-thick silicon nitride
387 membranes, the nanoparticles were baked at 100 °C for 12 hours in vacuum to eliminate any hydrocarbon
388 contamination. Both energy-dispersive X-ray and electron energy loss spectroscopy data show that the
389 nanoparticles were still in metallic form and were not oxidized during the experiment (Extended Data Fig.
390 1b-q).

391 **Data acquisition.** A set of tomographic tilt series were acquired from seven nanoparticles using the TEAM
392 0.5 microscope with the TEAM stage⁵⁴. Images were collected at 200 kV in ADF-STEM mode (Extended
393 Data Table 1). To minimize sample drift, four sequential images per tilt angle were measured with a dwell
394 time of 3 μs . To monitor any potential damage induced by the electron beam, we took 0° images before,
395 during and after the acquisition of each tilt series and ensured that no noticeable structural change was
396 observed for the seven nanoparticles. The total electron dose of each tilt series was estimated to be between
397 7×10^5 $\text{e}^-/\text{\AA}^2$ and 9.5×10^5 $\text{e}^-/\text{\AA}^2$ (Extended Data Table 1).

398 **Image pre-processing and denoising.** For each experimental tilt series, we performed the following
399 procedure for image post-processing and denoising.

400 i) Image registration. At each tilt angle, we used the first image as a reference and calculated normalized
401 cross-correlation between the reference and the other three images using a step size of 0.1 pixel⁵⁵. These
402 four images were aligned and summed to form an experimental image at that tilt angle.

403 ii) Scan distortion correction³⁸. Two steps were used to correct the scan distortion for the experimental
404 images. First, a set of low-magnification images were taken from nanoparticles and their positions were
405 fitted with a Gaussian. Based on the geometric relation of the nanoparticles at different angles, the scan coil
406 directions were calibrated to be perpendicular and equal in strength. Second, six high-magnification images
407 were taken from a multi-component metallic nanoparticle and scan distortion parameters were estimated
408 by minimizing the mean squared error of the common line of the six images. These scan distortion
409 parameters were applied to the experimental images.

410 iii) Image denoising. The experimental images contain mixed Poisson and Gaussian noise and were
411 denoised by the block-matching and 3D filtering (BM3D) algorithm⁵⁶, which has been demonstrated to be
412 effective in reducing noise in AET^{38,40,42}. The BM3D denoising parameters were optimized by the following
413 three steps. First, Poisson and Gaussian noise level were estimated from the experimental tilt series. Second,

414 several images were simulated based on a model nanoparticle, which has a similar size and elemental
 415 distribution as those of an experimental image. The same level of Poisson and Gaussian noise was added
 416 to the simulated images. Third, these noisy images were denoised by BM3D with different parameters. The
 417 denoising parameters corresponding to the largest cross-correlation coefficient between the denoised and
 418 the original images were chosen and applied to denoise the experimental images.

419 iv) Background subtraction and alignment. After denoising, a 2D mask was defined from each experimental
 420 image, which is slightly larger than the size of the nanoparticle. The background inside the mask was
 421 estimated by the discrete Laplacian in Matlab. After background subtraction, the experimental images of
 422 each tilt series were projected onto the tilt axis to produce a set of 1D curves (termed common lines). The
 423 images were aligned along the tilt axis by maximizing the cross-correlation between the common lines. The
 424 alignment of the images perpendicular to the tilt axis was achieved by the centre of mass method. The
 425 centres of mass of the images were calculated and the images were shifted so that all the centres of mass
 426 coincide with the origin. This image alignment method has been successfully used to achieve sub-pixel
 427 accuracy^{34,36,40-42}. The Matlab data of the raw, processed and aligned experimental images are provided in
 428 Supplementary Information.

429 **The REal Space Iterative REconstruction (RESIRE) algorithm.** After post-processing and denoising,
 430 the experimental images were reconstructed by the RESIRE algorithm. The algorithm iteratively minimizes
 431 an error function defined by,

$$432 \quad \varepsilon_{\theta}(O) = \frac{1}{2} \sum_{x,y} |\Pi_{\theta}(O)\{x,y\} - b_{\theta}\{x,y\}|^2 \quad (1)$$

433 where $\varepsilon_{\theta}(O)$ is an error function of a 3D object (O) at tilt angle θ , $\Pi_{\theta}(O)$ projects O to generate a 2D image
 434 at angle θ , b_{θ} is the experimental image at angle θ , and $\{x,y\}$ is the coordinates. The minimization is
 435 solved via the gradient descent,

$$436 \quad \nabla \varepsilon_{\theta}(O)\{u,v,w\} = \Pi_{\theta}(O)\{x,y\} - b_{\theta}\{x,y\} \quad \text{where} \quad \begin{bmatrix} u \\ v \\ w \end{bmatrix} = R_{\theta} \begin{bmatrix} x \\ y \\ z \end{bmatrix} \quad \text{for some } z \quad (2)$$

437 where ∇ represents the gradient and R_{θ} is the rotation matrix at tilt angle θ , which transforms coordinates
 438 $\{x,y,z\}$ to $\{u,v,w\}$. The j^{th} iteration of the RESIRE algorithm consists of the following four steps.

439 i) A set of images are calculated from the 3D object of the j^{th} iteration using a Fourier method. The 3D
 440 object is first padded with zeros by properly choosing an oversampling ratio⁵⁷. Applying the fast Fourier
 441 transform to the zero-padded object generates a 3D array in reciprocal space, from which a series of 2D
 442 Fourier slices are obtained at different tilt angles. These 2D Fourier slices are inverted to a set of images
 443 via the inverse Fourier transform.

444 ii) The error function defined in equation 1 is calculated between the computed and experimental images.

445 iii) The gradient of the error function is computed for every voxel using equation 2.

446 iv) The 3D object of the $(j+1)^{\text{th}}$ iteration is updated by,

$$447 \quad O^{j+1} = O^j - \frac{\Delta}{nN} \sum_{\theta} \nabla \varepsilon_{\theta}(O^j) \quad (3)$$

448 where Δ is the step size ($\Delta = 2$ was chosen for the reconstruction of our experimental data), n is the number
 449 of images and N is the dimension of each image ($N \times N$). $O^{j+1}\{u, v, w\}$ is used as an input for the $(j+1)^{\text{th}}$
 450 iteration.

451 The convergence of the algorithm is monitored by the R-factor,

$$452 \quad R = \frac{1}{n} \sum_{\theta} \frac{\sum_{x,y} |\Pi_{\theta}(O)\{x, y\} - b_{\theta}\{x, y\}|}{\sum_{x,y} |b_{\theta}\{x, y\}|} . \quad (4)$$

453 Usually, after several hundreds of iterations, the algorithm converges to a high-quality 3D reconstruction
 454 from a limited number of images. Both our numerical simulation and experimental results have indicated
 455 that RESIRE outperforms other iterative tomographic algorithms such as generalized Fourier iterative
 456 reconstruction⁵⁸ and simultaneous iterative reconstruction technique⁵⁹. By avoiding iterating between real
 457 and reciprocal space, RESIRE can be applied to general sample geometry such as thin films and extended
 458 objects. The details of the RESIRE algorithm will be reported in a follow-up paper.

459 For each aligned experimental tilt series, we first ran RESIRE for 200 iterations. From the initial
 460 3D reconstruction, we performed the angular refinement and spatial alignment for the experimental
 461 images^{40,58}. For each experimental image, we determined the corresponding three Euler angles of the 3D
 462 reconstruction. We sequentially scanned each of the three Euler angles with a small angular increment. At
 463 each scanning step, we projected the 3D reconstruction back to calculate an image. The experimental image
 464 was shifted along the x and y-axis and aligned with the calculated one. An error metric, defined as the
 465 difference between the calculated and experimental image, was computed. After scanning all the three Euler
 466 angles, three optimal Euler angles was found with the smallest error metric. This procedure was iterated for
 467 all the experimental images until there was not further improvement, producing a set of spatially aligned
 468 experimental images and refined tilt angles. Next, the background of each experimental image was re-
 469 evaluated and re-subtracted. Using these experimental images with the refined tilt angles (Extended Data
 470 Fig. 4a), we ran another 200 iterations of RESIRE to obtain the final 3D reconstruction of each experimental
 471 tilt series (Extended Data Table 1). The source codes of RESIRE are provided in Supplementary
 472 Information.

473 **Determination of 3D atomic coordinates and species.** From each final 3D reconstruction, the atomic
 474 coordinates and species were identified using the following procedure^{40,42}.

475 i) Each 3D reconstruction was upsampled by a factor of 3 using the spline interpolation, from which all the
 476 local maxima were identified. Starting from the highest intensity peak, polynomial fitting⁶⁰ was performed
 477 on a $0.8 \times 0.8 \times 0.8 \text{ \AA}^3$ ($7 \times 7 \times 7$ voxel) volume around each local maximum to locate the peak position. If the
 478 distance between the fitted peak position and existing potential atom positions is larger than or equal to 2
 479 \AA , it was listed as a potential atom. After repeating this step for all the local maxima, a list of potential atom
 480 positions was obtained. This method to trace the positions of potential atoms has previously been rigorously
 481 tested by using two independent experimental tilt series acquired from the same sample⁴².

482 ii) A 3D difference map was generated by taking the difference between the 3D reconstruction and the list
 483 of the potential atoms. Based on the difference map, we manually adjusted a very small fraction of the
 484 atoms (167 out of 18356), which has been routinely used in protein crystallography⁶¹.

485 iii) A K-mean clustering method^{40,42,62} was used to classify three types of atoms and non-atoms (Co and Ni
 486 as type 1, Ru, Rh, Pd and Ag as type 2, and Ir and Pt as type 3) based on the integrated intensity of a 0.8 \AA
 487 $\times 0.8 \text{ \AA} \times 0.8 \text{ \AA}$ volume around each potential atom position. An initial atomic model with 3D atomic
 488 coordinates was determined from each 3D reconstruction.

489 iv) Due to the missing wedge problem and noise in the experimental images, there is local intensity
 490 variation in each 3D reconstruction. A local reclassification was iteratively performed to refine the type 1,
 491 2 and 3 atoms. Each atom was defined as the centre of a 10-\AA -radius sphere. The average intensity
 492 distribution of type 1, 2 and 3 atoms was computed within the sphere. The L_2 norm of the intensity
 493 distribution between the centre atom and the average type 1, 2 and 3 atom was calculated. The centre atom
 494 was assigned to the type with the smallest L_2 norm. The procedure was iteratively repeated until there were
 495 no further changes. The source codes for 3D atom tracing and classification are provided in Supplementary
 496 Information.

497 **Refinement of 3D atomic coordinates.** The 3D atomic coordinates were refined by minimizing the error
 498 between the calculated and measured images using the gradient descent^{38,40,42}. Each atom was first fit with
 499 a 3D Gaussian function with a height H and a width B' , where H and B' were considered the same for the
 500 same type of atoms. A 3D atomic model was obtained by,

$$501 \quad O\{x, y, z\} = \sum_i H_i \exp \left[-\frac{|x - x_i|^2 + |y - y_i|^2 + |z - z_i|^2}{B_i'} \right] \quad (5)$$

502 where x_i , y_i , z_i , H_i and B_i' are the coordinates, height and standard deviation of the i^{th} atom, respectively,
 503 $|x - x_i|, |y - y_i|, |z - z_i| \leq \rho$, and ρ is a cut-off size of the 3D Gaussian function. From the 3D atomic
 504 model, a set of projection images were computed at different tilt angle θ by,

$$505 \quad \Pi_\theta(O)\{u, v\} = \sum_w \sum_i H_i \exp \left[-\frac{|u - u_i|^2 + |v - v_i|^2 + |w - w_i|^2}{B_i'} \right] \quad (6)$$

$$506 \quad \text{where } \begin{bmatrix} u_i \\ v_i \\ w_i \end{bmatrix} = R_\theta \begin{bmatrix} x_i \\ y_i \\ z_i \end{bmatrix} \quad \text{and} \quad |u - u_i|, |v - v_i|, |w - w_i| \leq \rho.$$

507 Substituting equation (6) into (1), an error function was calculated, from which the gradient descent method
 508 was used to search for the optimal atomic position at the $(j+1)^{\text{th}}$ iteration,

$$509 \quad \{x_i, y_i, z_i\}^{j+1} = \{x_i, y_i, z_i\}^j - \Delta \sum_\theta [\Pi_\theta(O)\{u, v\} - b_\theta\{u, v\}] \nabla_i [\Pi_\theta(O)\{u, v\}] \quad (7)$$

510 Where ∇_i is the spatial gradient operator with respect to the atomic position (x_i, y_i, z_i) . The iterative
 511 refinement process was terminated when the L_2 norm error could not be further reduced.

512 **3D precision estimation with multislice simulations.** A tilt series of 55 STEM images were calculated
 513 from the experimental 3D atomic model by using a fast multislice simulation software based on graphics
 514 processing unit⁶⁶. At each refined experimental angle (Extended Data Fig. 4a), the experimental 3D atomic
 515 model was placed in a cuboidal super cell and the super cell was divided into multiple 2-\AA -thick slices
 516 along the z -axis. The experiment parameters shown in Extended Data Table 1 (particle 1) were used for the
 517 multislice simulations. After using the parallel computing to perform the multislice simulations for all the
 518 angles, we calculated 55 multislice STEM images, each with 289×289 pixels and a pixel size of 0.347 \AA .

519 To account for the electron probe size and other incoherent effects, each multislice STEM image was
 520 convolved with a Gaussian kernel. Extended Data Fig. 4c and d show a representative experimental and
 521 multislice STEM image, respectively. An average R-factor between the 55 experimental and multislice
 522 images (defined in equation 4) was computed to be 14.96%, which, according to the crystallography
 523 standard⁶¹, represents a good agreement between the two sets of images.

524 From the 55 multislice STEM images with angular errors (Extended Data Fig. 4a), we performed
 525 the 3D reconstruction and angular refinement with RESIRE (Extended Data Fig. 4b). After applying the
 526 atomic tracing, classification and refinement procedure to the reconstruction, we obtained a new 3D atomic
 527 model of the sample, consisting of 8438, 6905 and 3138 type 1, 2, and 3 atoms, respectively. We identified
 528 7898, 6837, 3138 common pairs of type 1, 2 and 3 atoms, respectively, between the experimental and
 529 multislice atomic models based on the criterion of each common pair within a radius of 1.5 Å. The total
 530 common pairs of the three types of atoms are 17873, indicating that 97.37% of all atoms have been corrected
 531 identified. Extended Data Fig. 4d shows the distribution of the atomic deviation between all the common
 532 pairs with the root-mean-square deviation (i.e. 3D precision) of 21 pm.

533 **The local bond orientational order (BOO) parameters.** The local BOO parameters (Q_4 and Q_6) were
 534 calculated from the 3D atomic model of each nanoparticle using a method described elsewhere^{63,64}. The Q_4
 535 and Q_6 order parameters were computed up to the second shell with a shell radius set by the first valley in
 536 the PDF curve of the 3D atomic model. Figure 1f and Extended Data Fig. 2h-n show the distribution of the
 537 local BOO parameters of all the atoms in particles 1-7. To separate the amorphous structure from the crystal
 538 nuclei, we calculated the normalized BOO parameter, defined as $\sqrt{Q_4^2 + Q_6^2} / \sqrt{Q_{4\text{fcc}}^2 + Q_{6\text{fcc}}^2}$, where
 539 $Q_{4\text{fcc}}$ and $Q_{6\text{fcc}}$ are the Q_4 and Q_6 value for a perfect fcc lattice. The normalized BOO parameter is between
 540 0 and 1, where 0 means $Q_4 = Q_6 = 0$ and 1 represents a perfect fcc crystal structure. Based on the BOO
 541 parameters of a $\text{Cu}_{65}\text{Zr}_{35}$ metallic glass structure obtained from molecular dynamics simulations⁶⁵
 542 (Extended Data Fig. 2o), we chose the normalized BOO parameter = 0.5 as a cut-off to separate crystal
 543 nuclei from amorphous structure (red curves in Fig. 1f and Extended Data Fig. 2h-n).

544 **Characterization of the crystalline-amorphous interface.** The 3D surface of each crystal nucleus was
 545 defined by setting the normalized BOO parameter ≥ 0.5 . For every atom, the perpendicular distance to the
 546 3D surface of its closest crystal nucleus was calculated. If the atom is inside the nucleus, the distance is
 547 negative, otherwise it is positive. After counting all the atoms in the nanoparticle, a 1D curve was created
 548 to represent the normalized BOO parameter as a function of the distance. An exponential decay function
 549 $y = ae^{-x/d_c} + b$ was used to fit the 1D curve, where a and b are two constant, and d_c is the characteristic
 550 width of the crystalline-amorphous interface. For the crystal nuclei in the glass-forming nanoparticle, d_c
 551 was determined to be 3.69 Å, which is consistent with the molecular dynamics simulation of a poor glass
 552 former³⁰.

553 **PDF and partial PDF.** The PDF was calculated for the 3D atomic model of each nanoparticle using the
 554 following procedure. i) The distance of all atom pairs in each 3D atomic model was computed and binned
 555 into a histogram. ii) The number of atom pairs in each bin was normalized with respect to the volume of
 556 the spherical shell corresponding to each bin. iii) The histogram was scaled so that the PDF approaches one

557 for large separations. After plotting the PDF for each nanoparticle, the first valley of the PDF was used as
 558 the nearest neighbour cut-off distance to calculate the local BOO parameters (Fig. 1f and Extended Data
 559 Fig. 2h-n). By choosing the atoms in the glass-forming nanoparticle (particle 1) with the normalized BOO
 560 parameter < 0.5 , we applied the above procedure to plot the PDF (Fig. 1g). For type 1, 2 and 3 atoms, we
 561 identified six sets of atoms pairs (type 11, 12, 13, 22, 23 and 33) in the nanoparticle. For each set of atom
 562 pairs, we used the above procedure to calculate the partial PDF shown in Fig. 1h.

563 **Voronoi tessellation and the coordination number (CN).** The analysis of the Voronoi tessellation was
 564 performed by following the procedure published elsewhere⁶, where the surface atoms of the nanoparticle
 565 were excluded. To reduce the effect of the experimental and reconstruction error on Voronoi tessellation,
 566 those surfaces with areas less than 1% of the total surface area of each Voronoi polyhedron were removed⁹.
 567 From the Voronoi tessellation, each polyhedron is designated by a Voronoi index $\langle n_1, n_2, n_3, n_4, \dots \rangle$ with
 568 n_i denoting the number of i -edged faces and the CN was calculated by $\sum_i n_i$.

569 To examine the effect of the 3D precision of AET on the Voronoi tessellation, we used a $\text{Cu}_{65}\text{Zr}_{35}$
 570 metallic glass structure obtained from molecular dynamics simulations⁶⁵. A 3D atomic model was cropped
 571 from the structure to have the similar 3D shape and size to the experimental nanoparticle (particle 1). Our
 572 Voronoi analysis reveals that the ten most abundant Voronoi polyhedra in the atomic model are $\langle 0,0,12,0 \rangle$,
 573 $\langle 0,2,8,2 \rangle$, $\langle 0,2,8,1 \rangle$, $\langle 0,1,10,2 \rangle$, $\langle 0,3,6,4 \rangle$, $\langle 0,3,6,3 \rangle$, $\langle 0,1,10,4 \rangle$, $\langle 0,2,8,4 \rangle$, $\langle 0,1,10,3 \rangle$ and $\langle 0,0,12,3 \rangle$.
 574 Their corresponding fractions are 14.26%, 10.26%, 7.97%, 6.92, 4.58%, 4.14%, 4.01%, 3.41%, 2.97% and
 575 2.32%, respectively. After adding the experimental error (Extended Data Fig. 4e) to the atomic model, the
 576 corresponding fractions of these ten Voronoi polyhedra become 13.70%, 9.95%, 7.91%, 6.97%, 4.63%,
 577 4.08%, 3.57%, 3.42%, 2.89% and 2.19%, respectively. This analysis indicates that the 3D precision of AET
 578 has only a small effect on the Voronoi tessellation.

579 **Quantification of the chemical SRO.** We used the Warren–Cowley parameters (α_{lm}) to quantify the
 580 chemical SRO^{67,68},

$$581 \quad \alpha_{lm} = 1 - \frac{Z_{lm}}{\chi_m Z_l} \quad (8)$$

582 where $l, m = 1, 2$ or 3 , Z_{lm} is the partial CN of type m atoms around type l atoms, χ_m is the fraction of
 583 type m atoms, and Z_l is the total CN around type l atoms. After excluding the surface atoms, we estimated
 584 χ_1 , χ_2 and χ_3 to be 42.97%, 38.28% and 18.75%, respectively. Using the partial CNs (Extended Data Fig.
 585 5b), we calculated $\alpha_{11} = -0.11$, $\alpha_{12} = 0.1$, $\alpha_{13} = 0.05$, $\alpha_{21} = 0.02$, $\alpha_{22} = 0.01$, $\alpha_{23} = -0.07$, $\alpha_{31} = 0.03$, α_{32}
 586 $= -0.06$, and $\alpha_{33} = 0.06$, indicating that the type 11 and 23 bonds are favoured, but the type 12 and 33 bonds
 587 are unfavoured. These results are consistent with the observations that the type 23 bond is 0.06 Å shorter
 588 than the average type 2 and 3 bonds and the type 12 bond is 0.06 Å longer than the average type 1 and 2
 589 bonds (Fig. 1h).

590 **Determination of the solute centres and MROs.** A breadth-first-search algorithm^{69,70} was implemented
 591 to search for the solute centres and MROs using the following procedure. First, the algorithm identified the
 592 solute centres from type 3 atoms based on two criteria: i) each solute centre must fall within a 0.75 Å radius
 593 from an fcc, hcp, bcc or sc lattice point; and ii) each solute centre must have at least one neighbouring type
 594 3 atom within the second-coordination-shell distance. Second, the identified solute centres were sorted out

595 to generate a queue of the fcc-, hcp-, bcc- or sc-like MRO candidates. Third, starting from the largest MRO
596 candidate (i.e. with the most solute centres), each candidate was classified as an MRO if it has at least five
597 or more solute centres and none of the solute centres was already occupied by another MRO. If any solute
598 centres were already occupied, they were removed from the MRO candidate and the candidate was refitted
599 into the lattice vectors and added back into the queue. If two or more MRO candidates have the same
600 number of solute centres, the one with the smallest error of fitting the solute centres into the lattice vectors
601 was analysed first. This process was repeated until all the MROs were identified, where each solute centre
602 can only belong to no more than one MRO. To corroborate our analysis, we repeated the above steps with
603 a 1 Å and 0.5 Å radius cut-off and the corresponding MROs are shown in Extended Data Figs. 6 and 7,
604 respectively.

605 An attempt was also made in searching for icosahedral-like MROs. The breadth-first-search
606 algorithm^{69,70} was used to find the MROs that falls within a 0.75 Å radius from the 12 vertices of an
607 icosahedron. Because the icosahedron cannot be periodically packed in three dimensions, only the nearest
608 neighbour vertices were searched, making the largest possible MRO have 13 solute centres (1 central solute
609 centre plus 12 nearest neighbours). After performing the search, the resulting possible MROs have a mean
610 value of 3.9, meaning on average each solute centre is connected to only 3 others when constrained to an
611 icosahedron within the second coordination shell. Furthermore, although the largest possible MRO has 7
612 solute centres, none of these solute centres form 5-fold symmetry. We also repeated this analysis with a 1
613 Å radius cut-off. The mean value of solute centres becomes 4.5, the largest MRO has 8 solute centres, and
614 there are 19 5-fold symmetries. The source codes for identifying the MROs are provided in Supplementary
615 Information.

616 **Determination of the 3D atomic structure of an amorphous CuTa thin film.** The following procedure
617 was used to experimentally resolve the 3D atomic positions in the CuTa thin film.

618 i) Sample preparation. CuTa thin films were fabricated *in-situ* in the sample chamber of the spin polarized
619 low energy electron microscope (SPLEEM) at NCEM, where clean ultrahigh vacuum conditions remained
620 in the low 10^{-9} torr range. Using thermal evaporation, CuTa thin films were deposited on Si_3N_4 substrates,
621 which were maintained well below 150 K during sample fabrication. The growth rate of the thin films was
622 in the range of 0.1 – 1 atomic monolayer per minute. After the fabrication of the CuTa thin films, a very
623 thin carbon capping layer was deposited on the films to protect the samples from oxidation.

624 ii) Data acquisition. A tomographic tilt series was acquired from the CuTa thin film using TEAM I under
625 ADF-STEM mode at 300 kV. To mitigate the sample drift, two images at each tilt angle were taken and
626 then aligned to improve the signal-to-noise ratio. The tilt series consists of a total of 40 images with a tilt
627 range from -67.9° to 64.9° (Extended Data Fig. 8). As the CuTa film is thinner than ~ 6 nm, 40 experimental
628 images are sufficient to produce a good 3D reconstruction. The total electron dose of the dataset is 4.8×10^5
629 $\text{e}/\text{\AA}^2$. All the experimental parameters of the tilt series can be found in Extended Data Table 1.

630 iii) Image alignment. All the image pre-processing and denoising steps for the analysis of the CuTa thin
631 film are similar to those of the glass-forming nanoparticle, except for image alignment. We first used the
632 cross-correlation between the neighbouring images to roughly align the CuTa images. Next, we searched
633 for some reference markers, which can be either created by adding some small nanoparticles or based on

634 features in the sample. In this experiment, we chose an isolated region in the images and aligned them using
635 the centre of mass and common line method^{34,36}. After obtaining the 3D reconstruction, we further refined
636 the alignment by projecting the reconstruction back to generate images and comparing them with the
637 experimental ones. This process was repeated until no further improvement could be made.

638 iv) 3D reconstruction, atomic tracing and refinement. Using RESIRE, we first performed a large volume
639 reconstruction of the CuTa thin film from the aligned images. Based on the thickness variation of the thin
640 film, we applied scanning AET⁴¹ to conduct multiple local volume reconstructions and then patched them
641 together to produce a full 3D reconstruction. Scanning AET has been previously demonstrated to be
642 effective in improving the 3D reconstruction of 2D materials and/or thin film samples⁴¹. From the full 3D
643 reconstruction, we projected it back to generate images and use them to perform the angular refinement and
644 spatial alignment. We iteratively repeated the process until there were no further changes. After obtaining
645 the final 3D reconstruction, we traced the Cu and Ta atoms based on the integrated intensity difference
646 between the two types of atoms. The 3D atomic positions were refined to produce a final 3D atomic model
647 of the CuTa thin film (Extended Data Fig. 9).

648

649 **Data availability**

650 The raw and processed experimental data can be freely downloaded at [https://github.com/AET-](https://github.com/AET-MetallicGlass/Supplementary-Data-Codes)
651 [MetallicGlass/Supplementary-Data-Codes](https://github.com/AET-MetallicGlass/Supplementary-Data-Codes). The 3D atomic coordinates of the glass-forming nanoparticle
652 has been deposited in the Materials Data Bank (MDB, www.materialsdatbank.org) with the MDB ID:
653 NiRh00001.

654 **Code availability**

655 All the MATLAB source codes for the RESIRE reconstruction and data analysis of this work are freely
656 available at <https://github.com/AET-MetallicGlass/Supplementary-Data-Codes>.

657 51. Xu, Z., Sun, H., Zhao, X. & Gao, C. Ultrastrong fibers assembled from giant graphene oxide
658 sheets. *Adv. Mater.* **25**, 188-193 (2013).

659 52. Takeuchi, A. & Inoue, A. Quantitative evaluation of critical cooling rate for metallic glasses.
660 *Mater. Sci. Eng. A* **304-306**, 446-451 (2001).

661 53. Bordeenithikasem, P. et al. Determination of critical cooling rates in metallic glass forming alloy
662 libraries through laser spike annealing. *Sci Rep* **7**, 7155 (2017).

663 54. Ercius, P., Boese, M., Duden, T. & Dahmen, U. Operation of TEAM I in a user environment at
664 NCEM. *Microsc. Microanal.* **18**, 676-683 (2012).

665 55. Lewis, J. P. Fast normalized cross-correlation. *Vis. Interface* **95**, 120-123 (1995).

666 56. Dabov, K., Foi, A., Katkovnik, V. & Egiazarian, K. Image denoising by sparse 3-D transform-
667 domain collaborative filtering. *IEEE Trans. Image Process.* **16**, 2080-2095 (2007).

668 57. Miao, J., Sayre, D. & Chapman, H. N. Phase retrieval from the magnitude of the Fourier transform
669 of non-periodic objects, *J. Opt. Soc. Am. A* **15**, 1662-1669 (1998).

- 670 58. Pryor, A. et al. GENFIRE: a generalized Fourier iterative reconstruction algorithm for high-
671 resolution 3D imaging. *Sci. Rep.* **7**, 10409 (2017).
- 672 59. Gilbert, P. Iterative methods for the three-dimensional reconstruction of an object from
673 projections. *J. Theor. Biol.* **36**, 105-117 (1972).
- 674 60. Rogers, S. S., Waigh, T. A., Zhao, X. & Lu, J. R. Precise particle tracking against a complicated
675 background: polynomial fitting with Gaussian weight. *Phys. Biol.* **4**, 220–227 (2007).
- 676 61. Brünger, A. T. et al. Crystallography & NMR System: a new software suite for macromolecular
677 structure determination. *Acta Crystallogr. D* **54**, 905–921 (1998).
- 678 62. Lloyd, S. Least squares quantization in PCM. *IEEE Trans. Infor. Theory* **28**, 129-137 (1982).
- 679 63. Steinhardt, P. J., Nelson, D. R. & Ronchetti, M. Bond-orientational order in liquids and glasses.
680 *Phys. Rev. B* **28**, 784-805 (1983).
- 681 64. Lechner, W. & Dellago, C. Accurate determination of crystal structures based on averaged local
682 bond order parameters. *J. Chem. Phys.* **129**, 114707 (2008).
- 683 65. Yu, H. B. & Samwer, K. Atomic mechanism of internal friction in a model metallic glass. *Phys.*
684 *Rev. B* **90**, 144201 (2014).
- 685 66. Pryor, A., Ophus, C. & Miao, J. A streaming multi-GPU implementation of image simulation
686 algorithms for scanning transmission electron microscopy. *Adv. Struct. Chem. Imag.* **3**, 15 (2017).
- 687 67. Warren, B. E. *X-ray diffraction* (New York: Dover Publications Inc. 1990).
- 688 68. Cowley, J. M. X-Ray Measurement of order in single crystals of Cu₃Au. *J. Appl. Phys.* **21**, 24-29
689 (1950).
- 690 69. Lee, C. Y. An algorithm for path connections and its applications. *IEEE Trans. Electron.*
691 *Comput.* **EC-10**, 346-365 (1961).
- 692 70. Larsen, P. M., Schmidt, S. & Schiøtz, J. Robust structural identification via polyhedral template
693 matching. *Model. Simul. Mater. Sci. Eng.* **24**, 055007 (2016).

694

695 **Acknowledgements** We thank J. Ding for stimulating discussions, H. B. Yu for providing a molecular
696 dynamics simulated atomic model of the Cu₆₅Zr₃₅ metallic glass, and D. J. Kline and M. R. Zachariah for
697 assistance with the temperature measurements. This work was primarily supported by STROBE: A National
698 Science Foundation Science & Technology Center under Grant No. DMR 1548924. This work was also
699 partially supported by the U.S. Department of Energy, Office of Science, Basic Energy Sciences, Division
700 of Materials Sciences and Engineering under Award No. DE-SC0010378 (data acquisition and 3D image
701 reconstruction) and the NSF DMREF program under Award No. DMR-1437263. J.M. acknowledges partial
702 support from an Army Research Office MURI grant on Ab-Initio Solid-State Quantum Materials: Design,
703 Production and Characterization at the Atomic Scale. The ADF-STEM imaging with TEAM 0.5 was

704 performed at the Molecular Foundry, which is supported by the Office of Science, Office of Basic Energy
705 Sciences of the U.S. DOE under Contract No. DE-AC02—05CH11231.

706

707 **Author contributions** J.M. conceived the idea and directed the project; Yonggang Yao and L.H.
708 synthesized the samples; J.Z., P.E., A.K.S. and J.M. discussed and/or carried out the experiments; M.P.,
709 Yakun Yuan, A.R., S.J.O. and J.M. developed the RESIRE algorithm. Yao Yang, F.Z., Yakun Yuan, D.J.C.,
710 J.Z., D.S.K., X.T. and J.M. performed image reconstruction, atom tracing and classification, analysed the
711 data and/or interpreted the results; J.M., Yao Yang, J.Z., and F.Z. wrote the manuscript. All authors
712 commented on the manuscript.

713 **Competing interests** The authors declare no competing interests.

714 **Addition information**

715 **Supplementary Information** (with a link to the experimental data, RESIRE reconstruction and data
716 analysis source codes: <https://github.com/AET-MetallicGlass/Supplementary-Data-Codes>) accompanies
717 the paper.

718 **Correspondence and requests for materials** should be addressed to J.M. (miao@physics.ucla.edu).

719

720 **Extended Data legends**

721

722 **Extended Data Fig. 1 | Cooling rate measurement, energy-dispersive X-ray (EDX)**
723 **and electron energy loss spectroscopy (EELS) maps of the nanoparticles. a,** The
724 cooling rate for the average and maximum temperature curves was measured to be 51000
725 K/s (the slope of the red line) and 69000 K/s (the slope of the green line), respectively. **b,**
726 Low-resolution ADF-STEM image of the nanoparticles. EDX maps show the distribution
727 of Ni (**c**), Co (**d**), Ru (**e**), Rh (**f**), Pd (**g**), Ag (**h**), Ir (**i**) and Pt (**j**). **k,** The EDX spectrum of
728 all the elements shown in the images (**c-j**), where cps stands for counts per second. **l,**
729 Low-resolution ADF-STEM image of a large area, in which the white square indicates
730 the aggregation of several nanoparticles used for the EELS measurement. **m,** ADF-STEM
731 image of the white square region. **n-p,** EELS maps show the distribution of Co (**n**), Ni

732 (o) and O (p) in the region. q, EELS spectrum obtained from (n-p). No oxygen signal
733 was detected in the EELS map or spectrum. Scale bars, 20 nm in (b), 100 nm in (l) and
734 10 nm in (o).

735

736 **Extended Data Fig. 2 | Analysis of seven multi-component metallic nanoparticles. a-**
737 **g**, Representative ADF-STEM images of particles 1-7, respectively. Scale bar, 2 nm. **h-**
738 **n**, Local BOO parameters of all the atoms in particles 1-7, where the dashed red curves
739 correspond to the normalized BOO parameter = 0.5. The percentage on the top of each
740 panel shows the fraction of disordered atoms in each particle. **o**, Local BOO parameters
741 of a 3D atomic model cropped from a molecular dynamics simulated $\text{Cu}_{65}\text{Zr}_{35}$ metallic
742 glass⁶⁵ as a reference, from which the normalized BOO parameter = 0.5 (dashed red
743 curve) was chosen as a cut-off to separate crystal nuclei from amorphous structure. For a
744 fair comparison, the 3D atomic model was cropped to have the similar 3D shape and size
745 to the experimental nanoparticle (particle 1). **p-v**, PDFs of all the atoms in particles 1-7,
746 respectively. With the decrease of the fraction of disordered atoms in the nanoparticles,
747 the peaks in the PDFs become narrower and new peaks corresponding to different crystal
748 planes appear.

749

750 **Extended Data Fig. 3 | Experimental tomographic tilt series of the multi-component**
751 **glass-forming nanoparticle (particle 1).** 55 raw ADF-STEM images of the nanoparticle
752 with a tilt range from -69.4° to $+72.6^\circ$. The power spectra of the images are shown in the
753 insets, where the amorphous halo is visible. Some crystalline features are visible in
754 several experimental images and the 2D power spectra. Scale bar, 2 nm.

755

756 **Extended Data Fig. 4 | Angular errors in the experimental images and verification**
757 **of the experimental 3D atomic model using multislice simulations. a**, Angular errors
758 in the experimental images determined by the angular refinement procedure (Methods),
759 where the colour dots and lines represent the deviation of the three Euler angles (ϕ , θ and
760 φ) from the correct ones (0°) at each tilt angle. These angular errors were taken into
761 account in the multislice simulations. **b**, The angular errors were correctly refined in the
762 3D reconstruction of the 55 multislice images using RESIRE (Methods). After the angular
763 refinement, the largest error is only 0.2° . Comparison between a representative
764 experimental (after denoising) (**c**) and a multislice image (**d**) at 0° . To account for the
765 source size and incoherent effects, each multislice image was convolved with a Gaussian
766 function (Methods). **e**, Histogram of the deviation of the atomic positions between the
767 experimental atomic model and that obtained from 55 multislice images. The peak, mean
768 and root-mean-square deviation of the histogram are 6 nm, 15 nm and 21 pm,
769 respectively. Scale bar, 2 nm.

770

771 **Extended Data Fig. 5 | 3D distribution of the crystal nuclei in the glass-forming**
772 **nanoparticle, the partial CNs and the Voronoi polyhedra of the solute-centred**
773 **clusters. a**, 3D distribution of the atoms with the normalized BOO parameter ≥ 0.5 ,
774 revealing 15.46% of the total atoms forming crystal nuclei in the nanoparticle. **b**,
775 Normalized partial CNs of type 1, 2 and 3 atoms. **c**, 3D distribution of the 2682 solute
776 centres (red dots), which are between the first (3.78 \AA) and the second minimum (6.09 \AA)
777 of the PDF curve (Fig. 1g). **d**, Ten most abundant Voronoi polyhedra of the solute-centred
778 clusters.

779

780 **Extended Data Fig. 6 | Identification of MROs with a 1 Å radius cut-off. a**, Histogram
781 of the four types of MROs – fcc- (in blue), hcp- (in red), bcc- (in green) and sc-like (in
782 purple) – as a function of the size (i.e. the number of solute centres). **b**, The population
783 of the solute centre atoms for the four types of MROs. Representative fcc- (**c**), hcp- (**e**),
784 bcc- (**g**) and sc-like (**i**) MROs, containing 23, 18, 10 and 27 solute centres (large red
785 spheres), respectively. The solute centres are orientated along the fcc (**d**), hcp (**f**), bcc (**h**)
786 and sc (**j**) zone axes.

787

788 **Extended Data Fig. 7 | Identification of MROs with a 0.5 Å radius cut-off. a**,
789 Histogram of the four types of MROs – fcc- (in blue), hcp- (in red), bcc- (in green) and
790 sc-like (in purple) – as a function of the size. **b**, The population of the solute centre atoms
791 for the four types of MROs. Representative fcc- (**c**), hcp- (**e**), bcc- (**g**) and sc-like (**i**)
792 MROs, containing 15, 10, 8 and 8 solute centres (large red spheres), respectively. The
793 solute centres are orientated along the fcc (**d**), hcp (**f**), bcc (**h**) and sc (**j**) zone axes.

794

795 **Extended Data Fig. 8 | Tomographic tilt series of an amorphous CuTa thin film. a**,
796 ADF-STEM images of a portion of the CuTa thin film. The insets show the 2D power
797 spectra of the experimental images, in which the diffuse halos are clearly visible. Scale
798 bar, 2 nm.

799

800 **Extended Data Fig. 9 | Determination of the 3D atomic structure of the amorphous**
801 **CuTa thin film. a**, A large field of view of the amorphous CuTa. **b**, Magnified white
802 square region in (**a**). **c**, Average 2D power spectrum of all the experimental images. **d**,
803 3D atomic model of the portion of the CuTa thin film with a total of 1808 Cu (in gold)

804 and 12774 Ta (in blue) atoms, determined from the tilt series shown in Extended Data
805 Fig. 8a (Methods). As the CuTa film is thinner than ~6 nm, 40 experimental images are
806 sufficient to produce a good 3D reconstruction. **e**, A 2-Å-thick internal slice of the 3D
807 reconstruction of the amorphous CuTa thin film, showing the disordered atomic structure.
808 **f**, Local BOO parameters of the 3D atomic model, where only 0.47% of the total atoms
809 with the normalized BOO parameter ≥ 0.5 form crystal nuclei. **g**, PDF of the disordered
810 atoms with the normalized BOO parameter < 0.5 . Scale bars, 30 nm in **(a)**, 2 nm in **(b)**
811 and **(e)**.

812

813 **Extended Data Table 1 | AET data collection, processing, reconstruction, refinement**
814 **and statistics.** ^aThe R_1 -factor is defined as equation 5 in ref. 40. ^bThe R-factor is defined
815 in equation 4 in Methods.